ICES REPORT 12-14

April 2012

Simulation of Laminar and Turbulent Concentric Pipe Flows with the Isogeometric Variational Multiscale Method

by

Yousef Ghaffari Motlagh, Hyung Taek Ahn, Thomas J.R. Hughes, Victor M. Calo

The Institute for Computational Engineering and Sciences
The University of Texas at Austin
Austin, Texas 78712

Reference: Yousef Ghaffari Motlagh, Hyung Taek Ahn, Thomas J.R. Hughes, Victor M. Calo, Simulation of Laminar and Turbulent Concentric Pipe Flows with the Isogeometric Variational Multiscale Method, ICES REPORT 12-14, The Institute for Computational Engineering and Sciences, The University of Texas at Austin, April 2012.

Simulation of Laminar and Turbulent Concentric Pipe Flows with the Isogeometric Variational Multiscale Method

Yousef Ghaffari Motlagh[a], Hyung Taek Ahn[a,*], Thomas J.R. Hughes[b], Victor M. Calo[c]

[a]*School of Naval Architecture and Ocean Engineering,University of Ulsan, 102, Daehak-ro, Nam-gu Ulsan,680-749 ,Republic of Korea*
[b]*Institute for Computational Engineering and Sciences, The University of Texas at Austin, 201 East 24th street, 1 University Station C0200, Austin ,TX 78712,USA*
[c]*Earth and Environmental Science and Engineering, King Abdullah University of Science and Technology, P.O. Box 55455, Jeddah 21534, Saudi Arabia*

Abstract

We present an application of residual-based variational multiscale modeling methodology to the computation of laminar and turbulent concentric annular pipe flows. Isogeometric analysis is utilized for higher-order approximation of the solution using Non-Uniform Rational B-Splines (NURBS). The ability of NURBS to exactly represent curved geometries makes NURBS-based isogeometric analysis attractive for the application to the flow through annular channels. We demonstrate the applicability of the methodology to both laminar and turbulent flow regimes.

Keywords: Isogeometric analysis, NURBS, Concentric annular pipes, Transverse curvature, Incompressible Navier-Stokes equations

1. Introduction

Annular pipe flow is often encountered in engineering applications such as heat exchangers, combustion systems, and drilling operations in the oil and gas industry. Furthermore, annular pipe flow provides an insight into the problem of turbulent flows with curved walls. Usually, flow in a flat channel generates a symmetrical velocity profile and makes the positions of zero shear stress and maximum velocity coincident. However, the flow in a concentric annular channel does not result in a symmetric velocity profile. The asymmetric velocity profile results from the interaction of two flow zones with different Reynolds numbers based on the outer and inner cylinder radii. The transverse curvature alters significantly the overall characteristics of the wall bounded turbulence structures in the vicinity of the inner and outer walls by changing the radius ratio $\alpha = R_i/R_o$ where R_i and R_o are the inner and outer cylinder radii. In the case of annular pipe flow, two boundary layers exist and each has a different distribution of turbulent quantities. Moreover, pipe and channel flows are the limiting cases of annular pipe flow. For a small or high radius ratio, the profiles of turbulent quantities close to the inner cylinder are similar to those of the turbulent channel flow about a cylinder in axial flow. On the other hand, the profiles close to the outer wall are similar to those of turbulent pipe flow. In spite of the importance of the problem, the numerical simulation of turbulent pipe flow has received less interest than plane channel flow because of the numerical difficulties in precisely treating curved geometry.

A number of experiments on annular channel turbulence have been performed. Rehme [49] investigated turbulence in concentric annuli with small radius ratios for the Reynolds number range $Re = 2 \times 10^4$ to 2×10^5. Lawn and Elliott [43] performed turbulent annular channel flow experiments with three different radius ratios to study the effect

*Corresponding Author Tel: +82-52-259-2164; fax: +82-52-259-2836.
Email: htahn@ulsan.ac.kr.

of radius ratio. Nouri *et al.* [45] and Escudier *et al.* [22] performed an LDV experiment in concentric annuli for a radius ratio $\alpha = 0.5$. Those experiments predicted higher turbulence intensities near the inner wall than those near the outer wall when the turbulence characteristics are scaled by bulk mean velocity. On the other hand, only a few computations have been performed on turbulent flow in concentric annular channels. Azouz and Shirazi [4] evaluated several RANS models to predict the turbulent flow in concentric annuli and compared their results with the experimental data given by Nouri *et al.* [45]. Also, Chung *et al.* [15] performed a direct numerical simulation of annular channel flows at low Reynolds number. Finally, a fully developed turbulent concentric annular channel flow was investigated numerically by Liu *et al.* [44] using LES techniques employing a localized dynamic subgrid-scale (SGS) model.

Isogeometric analysis (IGA) is a computational mechanics technology that constructs single representations of exact geometry that is preserved under mesh refinement and polynomial degree elevation [1,2,3,5,6,8,12,13,17,18,19,20,21,23, 24,30,36,48,50,52]. The basic idea is to use in analysis the basis-function technology used in computational geometric representations. In modern Computer Aided Design (CAD) systems, Non-Uniform Rational B-splines (NURBS) are the dominant technology. When a NURBS model is constructed, the basis functions used to define the geometry can be systematically enriched by h-, p-, and/or k- refinement, without altering the geometry or its parameterization. Hence, an adaptive mesh refinement technique can be utilized independently without a link to the CAD database, in contrast with finite element methods. A distinguishing feature of isogoemetric analysis is k-refinement, in which the order of functions is increased together with their continuity. As a result, IGA allows for compactly supported higher-order and higher-continuity discretizations of complex geometries.

The variational multiscale (VMS) modeling methodology [38] provides a theoretical framework for general multi-scale problems in computational mechanics by separating the scales of interest in a predetermined number of groups, usually two, coarse (resolved) and fine (unresolved) scales, but three groups have been considered as well, namely, coarse resolved scales, fine resolved scales, and unresolved scales (i.e., the resolved scales are further distinguished [25,34,35,39]). VMS can be considered as a technique to take into account the effect of neglected unresolved fine scales on the coarse scales. The variational multiscale method was originally proposed as a theoretical justification of established stabilized methods, but has become a platform for the development of new computational technologies (see [1,6,9,25,33,34,35,37,39,42,52] for its application to turbulence modeling and simulation of complex flows).

The incompressible Navier-Stokes equations are the mathematical model for both laminar and turbulent flow. In this work we employ the residual-based VMS modeling approach recently proposed in [6]. The modeling paradigm encompasses the VMS theory of turbulence [25,28,29,33,34,35,38,39] and the numerical experience of stabilized methods [10,28,38] that are residual-based. VMS is not based on concepts emanating from flow physics, but rather concepts from the mathematical structure of the Navier-Stokes equations and a multiscale decomposition of the space of its admissible solutions. In this sense, VMS is a methodology for solving for all flows governed by the Navier-Stokes equations, be they laminar, turbulent or some combination of the two. This observation has been made previously, and the present work represents an opportunity to test it computationally on concentric annular channel flows. VMS modeling of flows entails an *a priori* additive scale separation that yields two equations which govern the dynamics of the coarse and fine scales. We identify the coarse scales with those resolved (captured) by the computational mesh, while fine unresolved (i.e., subgrid) scales are not properly captured by the mesh, but and their effect on the coarse scales needs to be accounted for. This is done by approximating the problems governing the unresolved scales with local problems that are linearized about the coarse scales and solved utilizing the concept of the "fine-scale Green's

function". The structure of the fine-scale Green's function was studied extensively in [37] and the interested reader is referred to this work for further details.

This paper is organized as follows. In Section 2 the strong and weak forms of the incompressible Navier-Stokes equations and the discrete VMS formulation are presented. In Section 3 our general approach to build an exact geometric model is presented. In Section 4 we present our numerical studies for a laminar flow. In Section 5 the results for turbulent concentric annular pipe flow at $Re = 8900$ are described. In Section 6 we summarize our observations and present our conclusions.

2. Incompressible Navier-Stokes equations and residual-based variational multiscale method

2.1. Strong and weak formulations

Let us start by recalling the incompressible Navier-Stokes equations. Let $\Omega \subset \mathbb{R}^d, d = 2, 3$, denote the spatial domain occupied by the fluid, and let $\Gamma = \partial\Omega$ be its boundary. Then

$$\frac{\partial \mathbf{u}}{\partial t} + \nabla \cdot (\mathbf{u} \otimes \mathbf{u}) + \nabla p = \nabla \cdot (2\nu \nabla^s \mathbf{u}) + \mathbf{f} \qquad in\ \Omega, t \in]0, T[, \tag{1}$$

$$\nabla \cdot \mathbf{u} = 0 \qquad in\ \Omega, t \in]0, T[, \tag{2}$$

where $\mathbf{u}$ is the velocity, $\mathbf{f}$ is the body force (per unit mass), ν is the kinematic viscosity, p is the pressure divided by the density and $\otimes$ denotes the tensor product (e.g., in component notation, $[u \otimes v]_{ij} = u_i v_j$). Equations. (1) and (2) are the balance of linear momentum and incompressibility constraint. These equations must be supplied with an initial condition of the form $\mathbf{u} = \mathbf{u}_0$ in Ω, $t = 0$ and a boundary condition which, for simplicity, will be taken as $\mathbf{u} = 0$ on Γ, $t \in]0, T[$. We also define $\nabla^s \mathbf{u}$ as follows:

$$\nabla^s \mathbf{u} = \frac{1}{2}(\nabla \mathbf{u} + (\nabla \mathbf{u})^T) \tag{3}$$

To formulate the weak statement of the problem, let $\mathscr{V}$ denote both the trial solution and weighting function spaces, which are assumed to be identical. We assume $\mathbf{U} = \{\mathbf{u}, p\} \in \mathscr{V}$ implies $\mathbf{u} = 0$ on Γ and $\int_\Omega p(t) d\Omega = 0$ for all $t \in]0, T[$. The variational formulation is stated follows: Find $\mathbf{U} \in \mathscr{V}$ such that $\forall \mathbf{W} = \{\mathbf{w}, q\} \in \mathscr{V}$

$$B(\mathbf{W}, \mathbf{U}) = L(\mathbf{W}) \tag{4}$$

where

$$B(\mathbf{W}, \mathbf{U}) = (\mathbf{w}, \frac{\partial \mathbf{u}}{\partial t})_\Omega - (\nabla \mathbf{w}, \mathbf{u} \otimes \mathbf{u})_\Omega + (q, \nabla \cdot \mathbf{u})_\Omega - (\nabla \cdot \mathbf{w}, p)_\Omega + (\nabla^s \mathbf{w}, 2\nu \nabla^s \mathbf{u})_\Omega \tag{5}$$

$$L(\mathbf{W}) = (\mathbf{w}, \mathbf{f})_\Omega \tag{6}$$

2.2. Residual-based variational multiscale method

We consider a direct-sum decomposition of $\mathscr{V}$ into coarse-scale and fine-scale subspace, $\mathscr{V}^h$ and $\mathscr{V}'$ respectively,

$$\mathscr{V} = \mathscr{V}^h \oplus \mathscr{V}' \tag{7}$$

$\mathscr{V}^h$ is assumed to be a finite-dimensional space, while $\mathscr{V}'$ is infinite-dimensional. The first step consists of the multiscale decomposition of the original fields,

$$B(\mathbf{W}^h, \mathbf{U}^h + \mathbf{U}') = L(\mathbf{W}^h) \tag{8}$$

$$B(\mathbf{W}', \mathbf{U}^h + \mathbf{U}') = L(\mathbf{W}') \tag{9}$$

where $\mathbf{U}^h = \{\mathbf{u}^h, p^h\}$ and $\mathbf{U}' = \{\mathbf{u}', p'\}$ stand for the coarse-scale (resolved-scale) and fine-scale (unresolved-scale) components of the solution, respectively. Equations (8) and (9) are the coarse- and fine-scale equations, respectively. The left-hand side of equation (8) consists of the following terms:

$$\begin{aligned} B(\mathbf{W}^h, \mathbf{U}^h + \mathbf{U}') &= (\mathbf{w}^h, \frac{\partial \mathbf{u}^h}{\partial t})_\Omega + (\mathbf{w}^h, \frac{\partial \mathbf{u}'}{\partial t})_\Omega \\ &- (\nabla \mathbf{w}^h, \mathbf{u}^h \otimes \mathbf{u}^h)_\Omega - (\nabla \mathbf{w}^h, \mathbf{u}^h \otimes \mathbf{u}')_\Omega \\ &- (\nabla \mathbf{w}^h, \mathbf{u}' \otimes \mathbf{u}^h)_\Omega - (\nabla \mathbf{w}^h, \mathbf{u}' \otimes \mathbf{u}')_\Omega \\ &+ (q^h, \nabla \cdot \mathbf{u}^h)_\Omega + (q^h, \nabla \cdot \mathbf{u}')_\Omega \\ &- (\nabla \cdot \mathbf{w}^h, p^h)_\Omega - (\nabla \cdot \mathbf{w}^h, p')_\Omega \\ &+ (\nabla^s \mathbf{w}^h, 2\nu \nabla^s \mathbf{u}^h)_\Omega + (\nabla^s \mathbf{w}^h, 2\nu \nabla^s \mathbf{u}')_\Omega \end{aligned} \tag{10}$$

We can rewrite (10) as follows:

$$\begin{aligned} B(\mathbf{W}^h, \mathbf{U}^h + \mathbf{U}') &= B(\mathbf{W}^h, \mathbf{U}^h) \\ &+ (\mathbf{w}^h, \frac{\partial \mathbf{u}'}{\partial t})_\Omega - (\nabla \mathbf{w}^h, \mathbf{u}^h \otimes \mathbf{u}')_\Omega \\ &- (\nabla \mathbf{w}^h, \mathbf{u}' \otimes \mathbf{u}^h)_\Omega - (\nabla \mathbf{w}^h, \mathbf{u}' \otimes \mathbf{u}')_\Omega \\ &+ (q^h, \nabla \cdot \mathbf{u}')_\Omega - (\nabla \cdot \mathbf{w}^h, p')_\Omega + (\nabla^s \mathbf{w}^h, 2\nu \nabla^s \mathbf{u}')_\Omega \end{aligned} \tag{11}$$

where

$$\begin{aligned} B(\mathbf{W}^h, \mathbf{U}^h) &= (\mathbf{w}^h, \frac{\partial \mathbf{u}^h}{\partial t})_\Omega - (\nabla \mathbf{w}^h, \mathbf{u}^h \otimes \mathbf{u}^h)_\Omega \\ &+ (q^h, \nabla \cdot \mathbf{u}^h)_\Omega - (\nabla \cdot \mathbf{w}^h, p^h)_\Omega + (\nabla^s \mathbf{w}^h, 2\nu \nabla^s \mathbf{u}^h)_\Omega \end{aligned} \tag{12}$$

The first term on the right-hand side of equation (11) is referred to as the Galerkin term, which is defined in (12); the second term is assumed to be equal to zero because the time derivative of $\mathbf{u}'$ is neglected, leading to a quasi-static modeling of the fine-scales. The third and fourth terms represent cross stress and the fifth term is the Reynolds stress. The fourth and fifth terms produced by the variational multiscale method are not accounted for in classical stabilization methods, such as SUPG and GLS, which only include the third term. The last term on the right-hand side of (11) is assumed to be zero due to an orthogonality condition induced by the Dirichlet projector. See [6] for further details and elaboration.

Now we focus on equation (9) which is the fine-scale equation. The left-hand side of (9) consists of the following terms:

$$\begin{aligned} B(\mathbf{W}', \mathbf{U}^h + \mathbf{U}') &= B(\mathbf{W}', \mathbf{U}^h) \\ &+ (\mathbf{w}', \frac{\partial \mathbf{u}'}{\partial t})_\Omega - (\nabla \mathbf{w}', \mathbf{u}^h \otimes \mathbf{u}')_\Omega \\ &- (\nabla \mathbf{w}', \mathbf{u}' \otimes \mathbf{u}^h)_\Omega - (\nabla \mathbf{w}', \mathbf{u}' \otimes \mathbf{u}')_\Omega \\ &+ (q', \nabla \cdot \mathbf{u}')_\Omega - (\nabla \cdot \mathbf{w}', p')_\Omega + (\nabla^s \mathbf{w}', 2\nu \nabla^s \mathbf{u}')_\Omega \end{aligned} \tag{13}$$

where

$$\begin{aligned} B(\mathbf{W}', \mathbf{U}^h) &= (\mathbf{w}', \frac{\partial \mathbf{u}^h}{\partial t})_\Omega - (\nabla \mathbf{w}', \mathbf{u}^h \otimes \mathbf{u}^h)_\Omega \\ &+ (q', \nabla \cdot \mathbf{u}^h)_\Omega - (\nabla . \mathbf{w}', p^h)_\Omega + (\nabla^s \mathbf{w}', 2\nu \nabla^s \mathbf{u}^h)_\Omega \end{aligned} \tag{14}$$

We can rearrange equation (9) by considering equation (13) in the following form:

$$B(\mathbf{W}', \mathbf{U}^h) - (\mathbf{W}', \mathbf{f}) + (\mathbf{w}', \mathscr{L}_{\mathbf{u}^h}\mathbf{u}' + (\nabla \cdot \mathbf{u}')(\mathbf{u}^h + \mathbf{u}'))_\Omega$$
$$(\mathbf{w}', \nabla \cdot \mathbf{u}'(\mathbf{u}^h + \mathbf{u}'))_\Omega + (q', \nabla \cdot \mathbf{u}')_\Omega - (\nabla \cdot \mathbf{w}', p')_\Omega = 0 \tag{15}$$

where

$$\mathscr{L}_{\mathbf{u}^h}\mathbf{u}' = \frac{\partial \mathbf{u}'}{\partial t} + \mathbf{u}^h \cdot \nabla \mathbf{u}' + (\nabla \cdot \mathbf{u}^h)\mathbf{u}' - \nabla \cdot (2\nu \nabla^s \mathbf{u}') \tag{16}$$

The first two terms in equation (15) can be expressed as

$$B(\mathbf{W}', \mathbf{U}^h) - (\mathbf{W}', \mathbf{f}) = (\mathbf{W}', \{\mathbf{r}_M, r_C\}) \tag{17}$$

where

$$\mathbf{r}_M(\mathbf{u}^h, p^h) = \frac{\partial \mathbf{u}^h}{\partial t} + \mathbf{u}^h \cdot \nabla \mathbf{u}^h + \nabla p^h - \nu \triangle \mathbf{u}^h - \mathbf{f}$$

$$r_C(\mathbf{u}^h) = \nabla \cdot \mathbf{u}^h \tag{18}$$

Equations (18) and (19) define the residuals of the coarse-scale equations. Finally, we can rewrite equation (15) as follows:

$$(\mathbf{w}', \mathscr{L}_{\mathbf{u}^h}\mathbf{u}' + \mathbf{u}' \cdot \nabla(\mathbf{u}^h + \mathbf{u}') + \mathbf{r}_M)_\Omega +$$
$$(\mathbf{w}', \nabla \cdot \mathbf{u}'(\mathbf{u}^h + \mathbf{u}'))_\Omega + (q', \nabla \cdot \mathbf{u}' + r_C)_\Omega - (\nabla \cdot \mathbf{w}', p')_\Omega = 0 \tag{19}$$

Since solving equation (20) is almost as daunting as solving the original Navier-Stokes system, several simplifying assumptions are considered [6]. These are that $\nabla \cdot \mathbf{u}' \approx 0$ and $\nabla \cdot \mathbf{w}' \approx 0$. Thus, equation (20) is reduced to :

$$(\mathbf{w}', \mathscr{L}_{\mathbf{u}^h}\mathbf{u}' + \mathbf{u}' \cdot \nabla(\mathbf{u}^h + \mathbf{u}') + \mathbf{r}_M)_\Omega = 0 \tag{20}$$

Equation (21) illustrates the fact that the fine scales are "driven" by the residual of the coarse-scale equation, $\mathbf{r}_M$. In addition to the above simplifying assumptions, $\mathbf{u}'$ is approximated through an algebraic model. We model the fine scales as in [16]:

$$\mathbf{U}' \approx -\boldsymbol{\tau}\mathbf{R}(\mathbf{U}^h) \tag{21}$$

where $\boldsymbol{\tau}$ is a 4×4 matrix and $\mathbf{R}(\mathbf{U}^h)$ is a 4×1 vector that collects momentum and continuity residual of the Navier-Stokes equations,

$$\mathbf{R}(\mathbf{U}^h) = \left\{\mathbf{r}_M^T(\mathbf{u}^h, p^h), r_C(\mathbf{u}^h)\right\}^T \tag{22}$$

We define $\boldsymbol{\tau}$ as follows:

$$\boldsymbol{\tau} = \begin{bmatrix} \tau_M I_{3\times 3} & \mathbf{O}_3 \\ \mathbf{O}_3^T & \tau_C \end{bmatrix} \tag{23}$$

where

$$\tau_M = \left(\frac{C_t}{\Delta t^2} + \mathbf{u}^h \cdot \mathbf{G}\mathbf{u}^h + C_I \nu^2 \mathbf{G} : \mathbf{G}\right)^{-1/2} \tag{24}$$

$$\tau_C = (\mathbf{g} \cdot \tau_M \ \mathbf{g})^{-1} \tag{25}$$

with $\mathbf{G}$ a second rank metric tensor

$$\mathbf{G} = \frac{\partial \boldsymbol{\xi}}{\partial \mathbf{x}}^T \frac{\partial \boldsymbol{\xi}}{\partial \mathbf{x}} \tag{26}$$

and $\mathbf{g}$ a vector obtained from the column sums of $\frac{\partial \boldsymbol{\xi}}{\partial \mathbf{x}}$, $\mathbf{g} = \{g_i\}$

$$g_i = \sum_{j=1}^{3} \left(\frac{\partial \xi_i}{\partial x_j}\right) \tag{27}$$

x and ξ denote the coordinates of elements in physical and parametric space, respectively. Also, Δt is the time step size and C_t and C_I are non-dimensional positive constants, independent of the mesh size. C_t is set to 4 and C_I is considered 36, 36×4 and 36×9 for linear, quadratic and cubic elements, respectively. Combining (8), (11) and (22), we obtain our discrete formulation: Find $\mathbf{U}^h$ such that $\forall \mathbf{W}^h$

$$B^{MS}(\mathbf{W}^h, \mathbf{U}^h) = L^{MS}(\mathbf{W}^h) \tag{28}$$

where

$$\begin{aligned} B^{MS}(\mathbf{W}^h, \mathbf{U}^h) &= B^G(\mathbf{W}^h, \mathbf{U}^h) \\ &+ \left(\mathbf{u}^h \cdot \nabla \mathbf{w}^h + \nabla q^h, \tau_M \mathbf{r}_M\right)_\Omega \\ &+ \left(\nabla \cdot \mathbf{w}^h, \tau_C r_C\right)_\Omega \\ &+ \left(\mathbf{u}^h \cdot (\nabla \mathbf{w}^h)^T, \tau_M \mathbf{r}_M\right)_\Omega \\ &- \left(\nabla \mathbf{w}^h, \tau_M \mathbf{r}_M \otimes \tau_M \mathbf{r}_M\right)_\Omega \end{aligned} \tag{29}$$

$$L^{MS}(\mathbf{W}^h) = (\mathbf{w}^h, \mathbf{f})_\Omega \tag{30}$$

and

$$\begin{aligned} B^G(\mathbf{W}^h, \mathbf{U}^h) &= (\mathbf{w}^h, \frac{\partial \mathbf{u}^h}{\partial t})_\Omega + (\nabla^s \mathbf{w}^h, 2\nu \nabla^s \mathbf{u}^h)_\Omega - (\nabla \mathbf{w}^h, \mathbf{u}^h \otimes \mathbf{u}^h)_\Omega \\ &+ (q^h, \nabla \cdot \mathbf{u}^h)_\Omega - (\nabla \cdot \mathbf{w}^h, p^h)_\Omega \end{aligned} \tag{31}$$

The superscripts MS and G stand for multiscale and Galerkin, respectively. Now, we consider the roles of the different terms in equation (30). The first term on the right-hand side of (30), defined in (32), is the Galerkin term; the next two terms are classical stabilization terms; and the last two terms are the additional terms produced by the variational multiscale method. From this perspective, classical stabilization methods, such as SUPG and GLS (see [38]), are viewed as only stepping stones toward the full variational multiscale method.

The generalized–α method [14, 40] is employed to integrate the governing equations in time. This leads to a nonlinear system of equations to be solved at each time step for which we employ a Newton-Raphson procedure with a two-stage predictor-multicorrector algorithm (see [6] for further details).

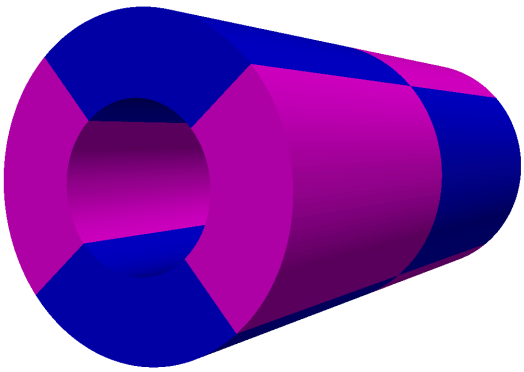

Figure 1: Exact geometric model of flow domain between concentric circular cylinders generated from quadratic NURBS elements.

3. Geometric model construction and basis functions for analysis

Quadratic and higher-order NURBS are capable of exactly representing all conic sections and are employed to develop exact geometric models of the annular cylindrical domain. There are several constructs that can be used for this purpose. The one we have utilized employed a decomposition of the solid annulus into patches, as illustrated in Figure 1. The physical dimensions are an inner radius $R_i = 2$, an outer radius $R_o = 4$ and length $L = 18$. Within each patch, quadratic NURBS are C^1-continuous and cubic NURBS are C^2-continuous, but in both cases only C^0-continuity is achieved between patches. This is necessary to exactly represent the cylindrical geometry. For background and illustration of the construction, the interested reader is referred to [18, 46]. See the Appendix for the definitions of all parameters used in the present model.

The basis functions used to represent flow variables (i.e., velocity and pressure) in the analyses are not the same as used to construct the geometry. The objective is to form smooth periodic bases in the axial and cylindrical directions. This can also be accomplished in several ways. The procedure we used is to start with smooth basis functions within each patch that are only C^0-continuous across patch interfaces and then apply constraint conditions that render them equally smooth across interfaces. The idea is schematically illustrated in Figure 2 for quadratic NURBS. A globally C^1-continuous basis is attained thereby. Proceeding analogously, a C^2-continuous basis may be constructed for cubic NURBS.

In one case, the laminar flow calculation of the next section, we also consider a standard trilinear hexahedral finite element mesh for both the geometry and flow variables. In this case the geometry is only approximate in that the cylindrical surfaces are approximated by flat rectangular facets.

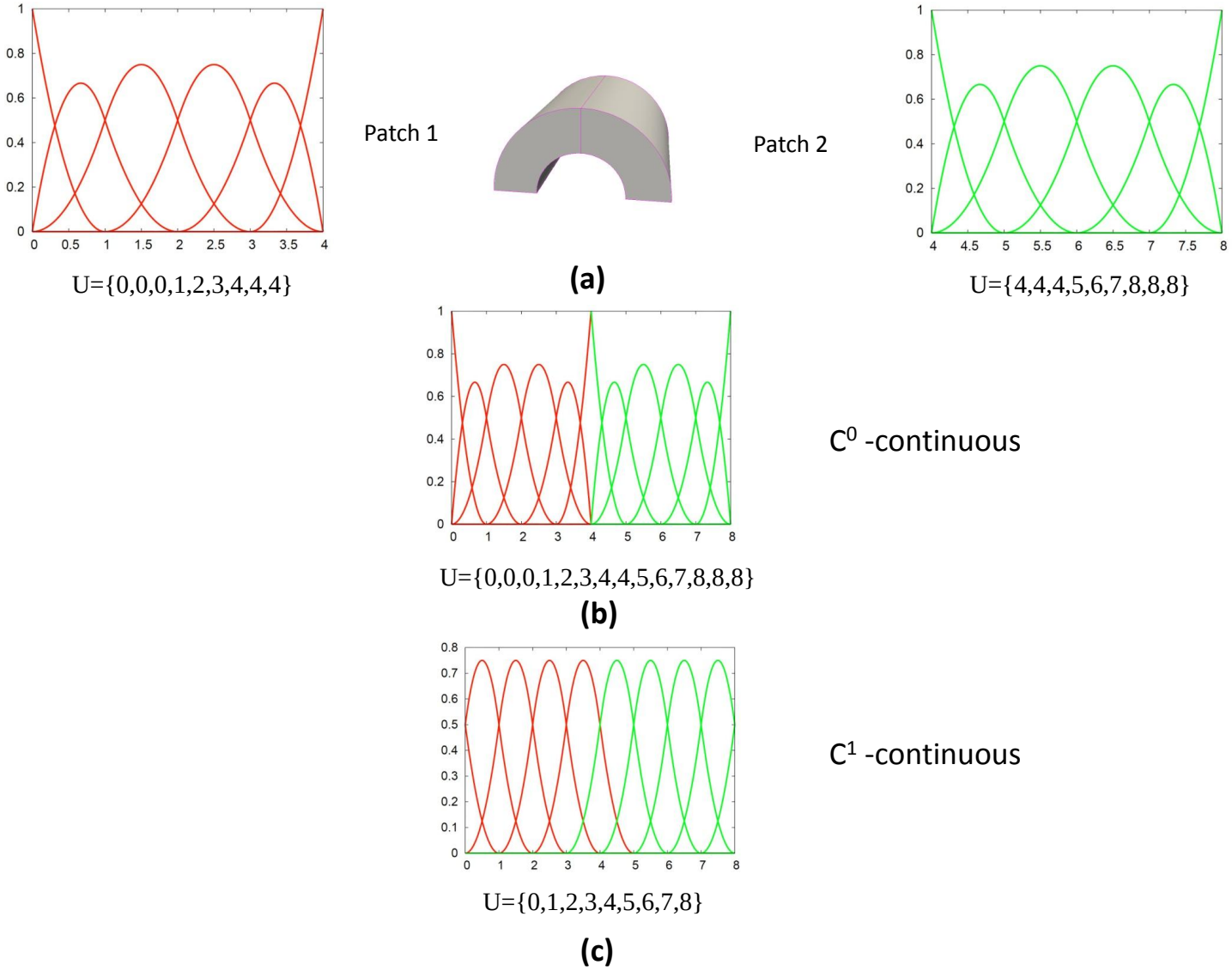

Figure 2: Improving continuity of quadratic NURBS between adjacent patches. (a) Adjacent patches constructed from open knot vectors. (b) Assembly of the patches into one patch that is only C^0-continuous at the interface of the two original patches. (c) C^1-continuous basis functions, constructed by applying appropriate constraints to (b). The end result is a C^1-continuous basis. C^2-continuity is achieved for cubic NURBS.

4. Laminar flow

This section describes a laminar verification of the numerical formulation. The flow is chosen as a test case because the exact solution is available to compare with the numerical results. Mesh refinement studies are performed for each order of solution approximation utilized, namely linear, quadratic, and cubic basis functions.

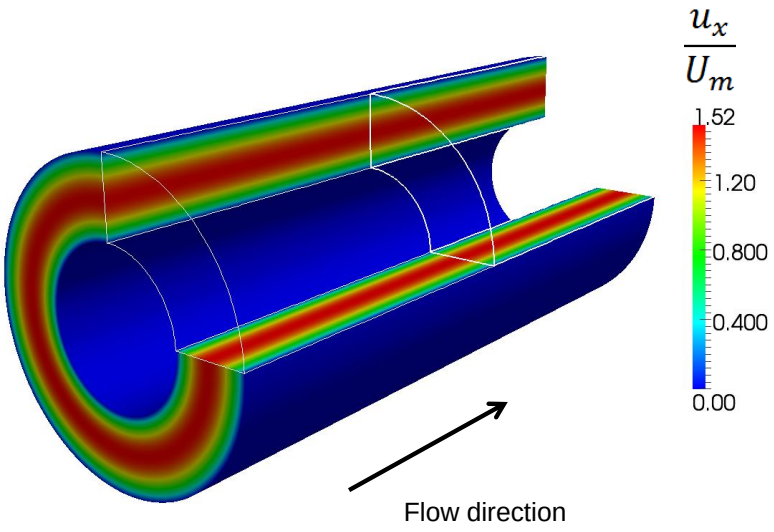

Figure 3: Laminar flow, snapshot of velocity contours for $Re = 0.004$, based on bulk-flow Reynolds number.

4.1. Problem setup

The flow domain is illustrated in Figure 3. A no slip Dirichlet boundary condition is set at the walls. The flow is driven by a constant pressure gradient, f_x, acting in the stream-wise direction. The values of the kinematic viscosity ν and the forcing f_x are set to 10^3 and 3.0, respectively.

4.2. Numerical results

The computations were performed on 16^3, 32^3 and 64^3 elements. We employ C^0-continuous linear finite elements, and C^1-continuous quadratic and C^2-continuous cubic NURBS. For all orders, the number of basis functions is equal to the number of elements in the stream-wise and circumferential directions. In the wall-normal direction, due to the open knot vector construction, the number of basis functions is $n + p$, where n is the number of elements in the wall-normal direction and p is the polynomial order. Our numerical results are compared with the analytical solution, which is given in [51], namely,

$$u = \frac{1}{4\nu}\Big(-\frac{dp}{dx}\Big)\Big({R_o}^2 - R^2 + \frac{{R_o}^2 - {R_i}^2}{\ln(R_i/R_o)}\ln\frac{R_o}{R}\Big) \tag{32}$$

The rates of convergence of the error measured in the L^2-norm of velocity versus mesh parameter, are presented in Figure 4. As may be seen in Figure 4, the slopes of the lines related to linear, quadratic and cubic approximations are approximately

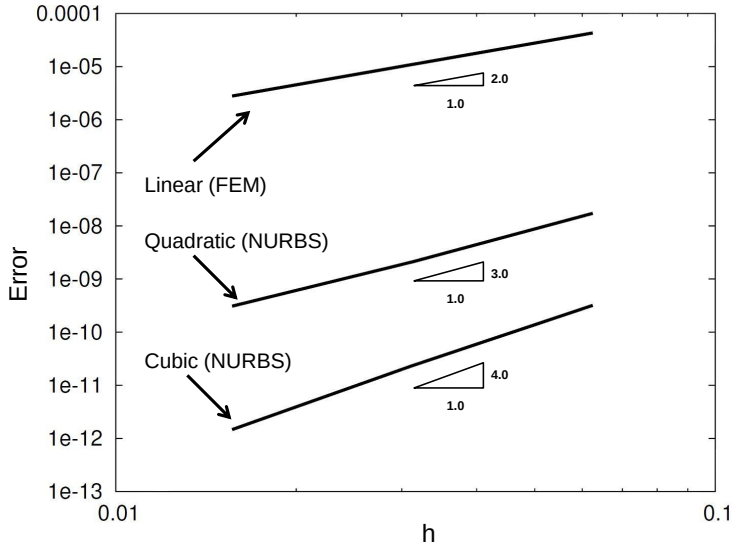

Figure 4: Convergence of the error in the L^2-norm of the velocity for linear finite elements, and quadratic and cubic NURBS discretizations.

two, three and four, indicating second-, third- and fourth-order accuracy, respectively. These results represent optimal rate of convergence in each case.

5. Turbulent flow in concentric annuli

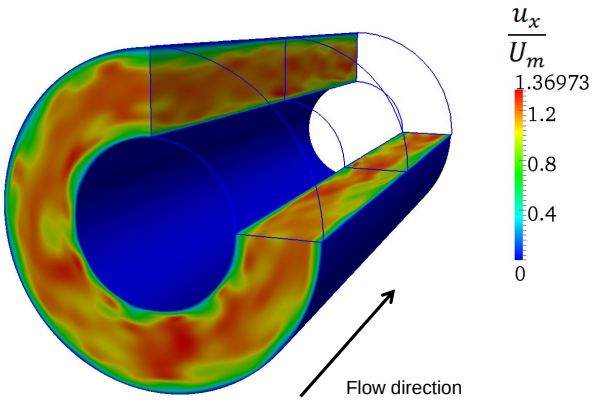

Figure 5: Turbulent flow; snapshot of velocity contours at $Re = 8900$, based on bulk-flow Reynolds number.

We conduct numerical experiments for the turbulent concentric annulus flow at bulk-flow Reynolds number of 8900 for the full domain, Figure 5. To assess the accuracy of our methodology, we compare our results to DNS data from Chung *et al.* [15] and Kim *et al.* [41].

5.1. Problem setup

The flow is driven by a pressure gradient, f_x, acting in the stream-wise direction. The value of kinematic viscosity ν is set to 4.49438×10^{-4} and, in order to maintain a constant flow rate, the forcing f_x is adjusted. Quadratic NURBS are utilized in all

the computations [30]. We perform our simulations using a sequence of h-refined meshes to assess the convergence properties of the numerical methodology. The continuity of the basis functions is kept at C^1, which is the maximal continuity achievable for a quadratic NURBS discretization. We note that at each level of refinement, quadratic NURBS capture the problem geometry exactly. The coarsest mesh computations were performed on a mesh of $64 \times 16 \times 16$ elements in the circumferential, radial and axial directions, respectively. With each h-refinement step we double the number of elements in each parametric direction to achieve our finest discretization of $256 \times 64 \times 64$ elements. A uniform mesh is used in the circumferential and axial directions. In the radial direction, the meshes are obtained by distributing the knots according to a hyperbolic tangent function to better capture the boundary layer turbulence.

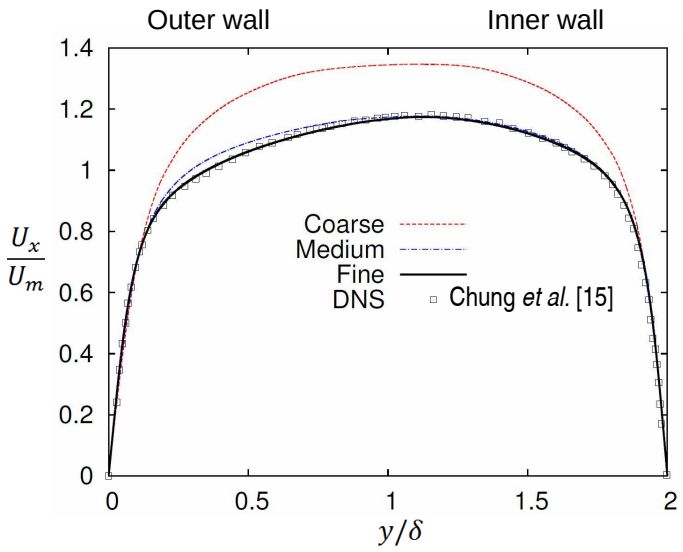

Figure 6: Mean axial velocity distribution normalized by the bulk velocity, U_m, at $Re = 8900$.

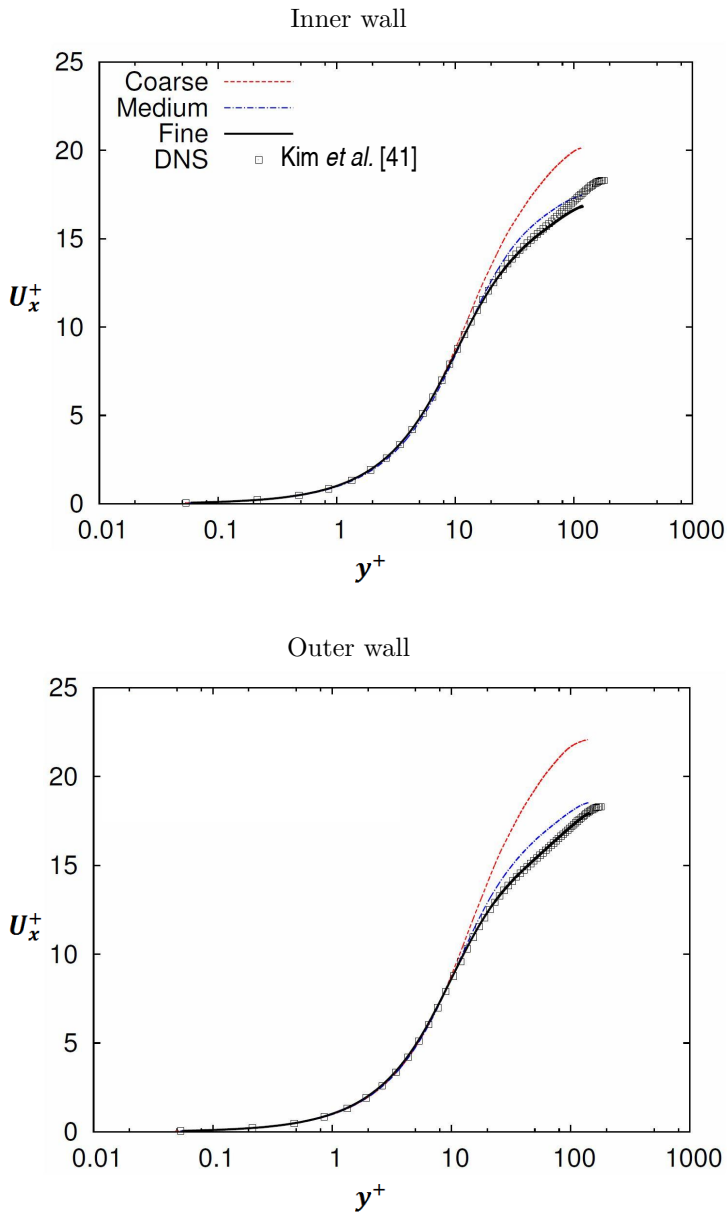

Figure 7: Inner and outer wall mean velocity distributions at $Re = 8900$ computed using quadratic NURBS: h-refinement interpretation of results. Here $U_x^+ = \frac{U_x}{u_\tau}$ and $y^+ = \frac{y u_\tau}{\nu}$.

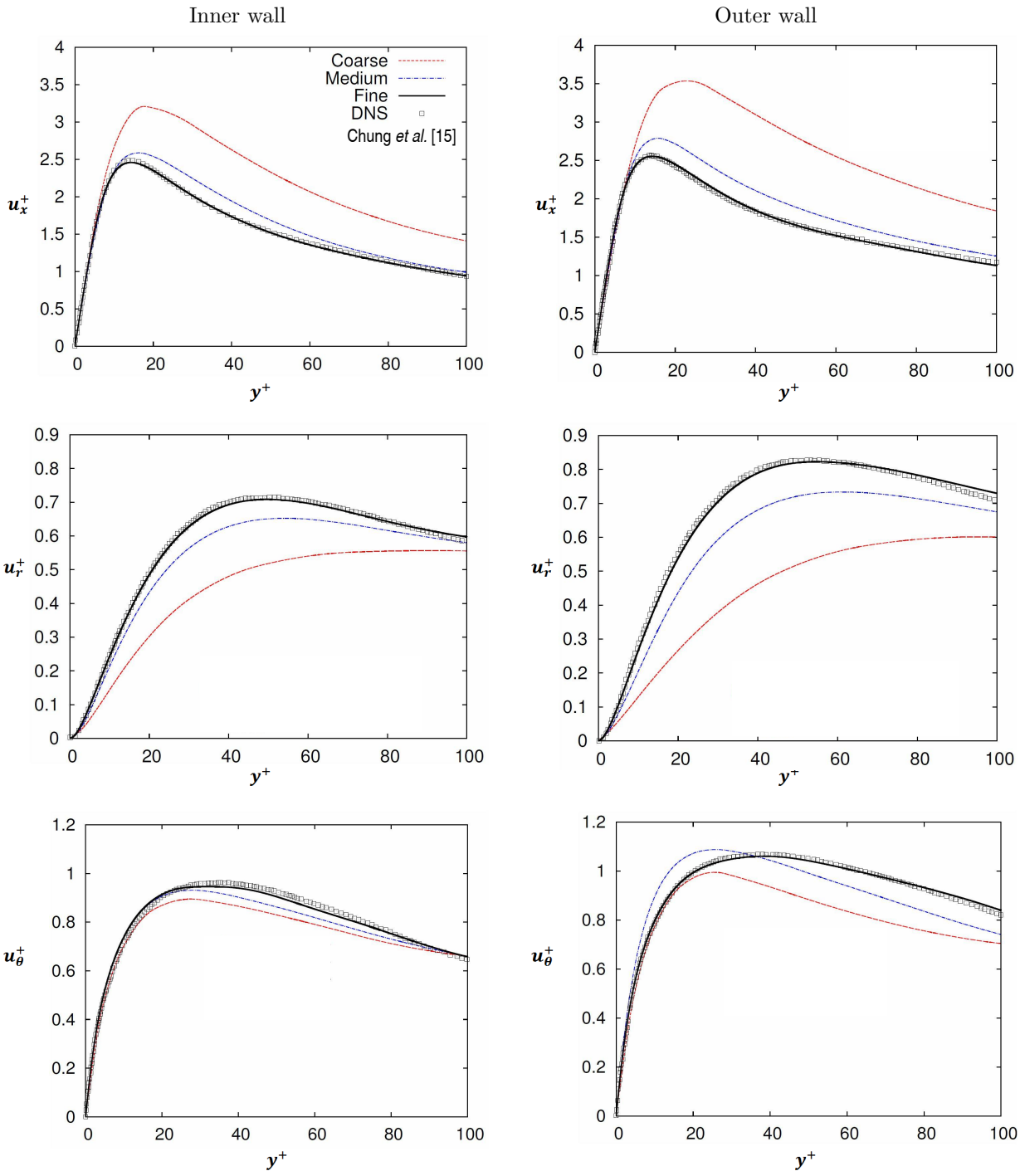

Figure 8: Left graphs from top to bottom show axial, radial and circumferential rms velocity fluctuations at the inner wall at $Re = 8900$, while the right graphs show the statistics at the outer wall. Quadratic NURBS are used in all cases.

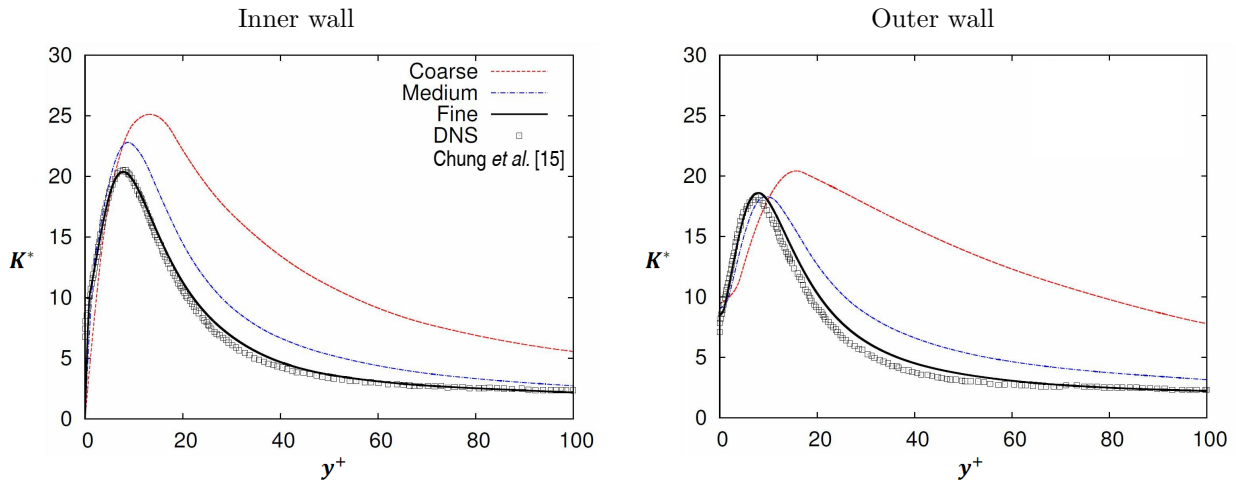

Figure 9: Inner and outer wall energy partition parameter $K^* = \frac{2\overline{u_x^2}}{\overline{u_r^2}+\overline{u_\theta^2}}$.

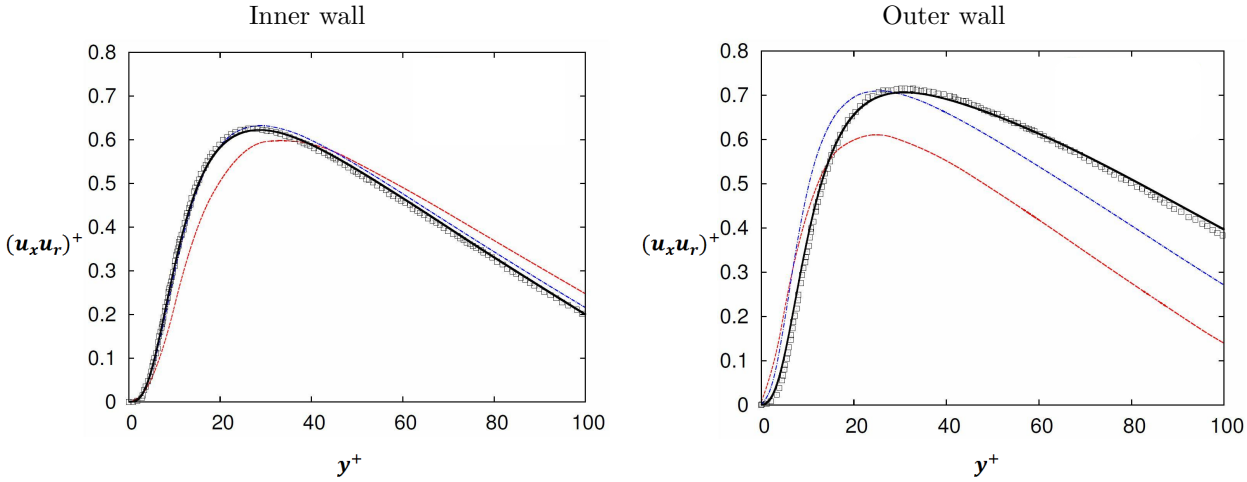

Figure 10: Inner and outer wall Reynolds shear stress in wall coordinates.

5.2. Numerical results

Numerical results for the test case are reported in the form of statistics of the mean stream-wise velocity and root-mean-square (rms) velocity fluctuations. Statistics are obtained by sampling the solution fields at the mesh knots and averaging in the stream-wise and circumferential directions as well as in time. Comparison of the mean velocity, normalized by the bulk velocity, is presented in Figure 6. Agreement with the DNS data is seen to be quite satisfactory. Note that the position of the maximum velocity is skewed toward the inner wall. The velocity profile in wall units is presented in Figure 7. For the finest mesh, a slight discrepancy is seen between the inner wall results and the DNS (Kim *et al.* [41]) for $y^+ > 100$, while the outer wall results are almost identical to the DNS. The fluctuating velocities are presented in Figure 8. A comparison between the inner and outer walls indicates that turbulent intensities of the inner wall are smaller than those of the outer wall. The smaller turbulent kinetic energy near the inner wall is due to the transverse curvature effect. Since the surface area of the inner wall is smaller than that of the outer wall, the inner wall supplies less turbulent kinetic energy than the outer wall to the same volume of flow. To reveal the altered energy redistribution, the energy partition parameter $K^* = \frac{2\overline{u_x^2}}{\overline{u_r^2}+\overline{u_\theta^2}}$ is employed and the results are shown in Figure 9. This is a measure of the relative contribution to the turbulent kinetic energy of the stream-wise turbulence

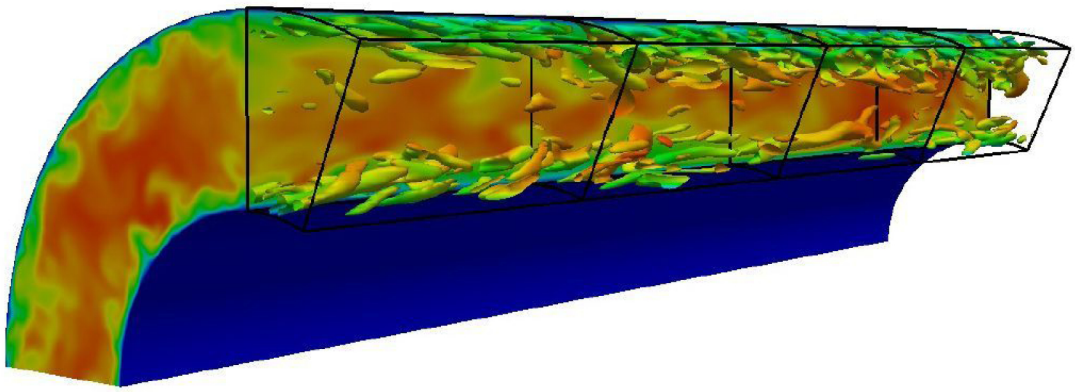

Figure 11: Turbulent concentric annular channel flow at $Re = 8900$. Isosurfaces of coherent structures at instantaneous time (Q-criterion, $Q = 0.3$) of fine mesh, contoured by stream-wise velocity.

intensity and intensities normal to the mean flow. Profiles of the Reynolds shear stress are displayed in Figure 10. It is seen that the Reynolds shear stress near the outer wall is larger than that near the inner wall, like the rms distributions of velocity fluctuations in Figure 8. Figure 11 shows an instantaneous isosurface of Q, where

$$Q = \frac{1}{2}(\|\Omega\|^2 - \|S\|^2) \tag{33}$$

and $\|S\| = \mathrm{tr}(SS^T)$ and $\|\Omega\| = \mathrm{tr}(\Omega\Omega^T)$. The tensors $S_{ij} = \frac{1}{2}(u_{i,j} + u_{j,i})$ and $\Omega_{ij} = \frac{1}{2}(u_{i,j} - u_{j,i})$ are the symmetric and skew–symmetric components of the velocity gradient tensor, $\bigtriangledown u$.

For the results presented in Figure 7-11, the following observations may be made. The coarse mesh is incapable of quantitatively accurate flow results. The medium mesh results are quite reasonable and might be considered of the caliber of a good LES model. The fine mesh gives very accurate results of near DNS quality. The convergence behavior is quite consistent in that clearly visible improvements occur from coarse to medium to fine meshes. It has been previously suggested that VMS provides a stable and accurate pathway to DNS results as meshes are systematically refined, and these results corroborate that claim.

We also wish to emphasize that exactly the same VMS methodology, in fact the same code, with no differences whatsoever, was used for both the laminar and turbulent calculations. The good results obtained in both cases supports the viability of VMS as a general methodology for computing solutions of the Navier-Stokes equations, be they laminar, turbulent or a combination thereof.

6. Summary and Conclusions

In this paper we have studied the behavior of the variational multiscale (VMS) method and isogeometric analysis (IGA) in the computation of laminar and turbulent concentric annular channel flows governed by the incompressible Navier-Stokes equations. In the laminar case we observed rapid, and in fact optimal, rates of convergence for linear finite elements, and quadratic and cubic NURBS. We note that NURBS of quadratic and higher order facilitate the construction of exact cylindrical geometric domains. The basis functions for flow variables are the same as those used in the geometry construction, a feature of IGA.

In the turbulent case we observed consistent convergence behavior of standard statistical measures across coarse, medium and fine meshes utilizing quadratic NURBS. The medium mesh results were of the level of accuracy of a good LES calculation and the fine mesh results were especially accurate, of almost DNS quality.

Exactly the same procedures and code were used in all calculations, supporting the hypothesis that the variational multiscale method is a general and accurate approach for solving the Navier-Stokes equations in all flow regimes. In the turbulent regime, VMS exhibits features similar to an LES turbulence model, but achieves rapid convergence to a DNS. In the laminar regime, VMS behaves like a higher-order accurate, residual-driven stabilized method. We believe these are distinguishing and advantageous features of VMS when compared with classical LES turbulence modeling methods.

Acknowledgments

This research was supported by WCU (World Class University) program through the National Research Foundation of Korea funded by the Ministry of Education, Science and Technology(#R33-10150), and also Basic Science Research Program through the National Research Foundation of Korea funded by the Ministry of Education, Science and Technology(#2009-0065381,#2010-0004606). The authors would like to acknowledge the support from KISTI supercomputing center through the strategic support program for the supercomputing application research(#KSC-2010-C2-0013).

Appendix A. Geometry construction.

The cylinder shown in Figure 1 has an inner radius of $R_i = 2$, and an outer radius of $R_o = 4$. The length of the cylinder is $L = 18$. Quadratic NURBS are used in all direction. The u_3 coordinate traverses the circumferential direction; the u_2 coordinate traverses the thickness, and the u_1 coordinate traverses the length. Table A.1 represents the knot vectors for the 8 patches.

Table A.1: Knot vectors for cylindrical solid

Patch no.	U_1	U_2	U_3
1	{0,0,0,1,1,1}	{0,0,0,1,1,1}	{0,0,0,1,1,1}
2	{1,1,1,2,2,2}	{0,0,0,1,1,1}	{0,0,0,1,1,1}
3	{0,0,0,1,1,1}	{0,0,0,1,1,1}	{1,1,1,2,2,2}
4	{1,1,1,2,2,2}	{0,0,0,1,1,1}	{1,1,1,2,2,2}
5	{0,0,0,1,1,1}	{0,0,0,1,1,1}	{2,2,2,3,3,3}
6	{1,1,1,2,2,2}	{0,0,0,1,1,1}	{2,2,2,3,3,3}
7	{0,0,0,1,1,1}	{0,0,0,1,1,1}	{3,3,3,4,4,4}
8	{1,1,1,2,2,2}	{0,0,0,1,1,1}	{3,3,3,4,4,4}

The control net and weights are given in Tables A.2 - A.9 . Rational solid basis functions are defined by combining the weights and one-dimensional basis functions using (A.1),

$$R^{p,q,r}_{i,j,k}(u_1,u_2,u_3) = \frac{N_{i,p}(u_1)M_{j,q}(u_2)L_{k,r}(u_3)w_{i,j,k}}{\sum_{\hat{i}=0}^{n}\sum_{\hat{j}=0}^{m}\sum_{\hat{k}=0}^{l} N_{\hat{i},p}(u_1)M_{\hat{j},q}(u_2)L_{\hat{k},r}(u_3)w_{\hat{i}\hat{j}\hat{k}}} \tag{A.1}$$

The number of control points are n, m, and l in the axial, radial and circumferential directions, repectively. The N, M, L, w represent the basis functions in each direction and the weight, and p, q, r are the polynomial orders in each direction.

Table A.2: Control points and weights for cylindrical solid, patch no.1

j	k	$B_{0,j,k}$	$B_{1,j,k}$	$B_{2,j,k}$	$w_{0,j,k}$	$w_{1,j,k}$	$w_{2,j,k}$
0	0	(0,0,2)	(9/2,0,2)	(9,0,2)	1	1	1
1	0	(0,0,3)	(9/2,0,3)	(9,0,3)	1	1	1
2	0	(0,0,4)	(9/2,0,4)	(9,0,4)	1	1	1
0	1	(0,2,2)	(9/2,2,2)	(9,2,2)	$1/\sqrt{2}$	$1/\sqrt{2}$	$1/\sqrt{2}$
1	1	(0,3,3)	(9/2,3,3)	(9,3,3)	$1/\sqrt{2}$	$1/\sqrt{2}$	$1/\sqrt{2}$
2	1	(0,4,4)	(9/2,4,4)	(9,4,4)	$1/\sqrt{2}$	$1/\sqrt{2}$	$1/\sqrt{2}$
0	2	(0,2,0)	(9/2,2,0)	(9,2,0)	1	1	1
1	2	(0,3,0)	(9/2,3,0)	(9,3,0)	1	1	1
2	2	(0,4,0)	(9/2,4,0)	(9,4,0)	1	1	1

Table A.3: Control points and weights for cylindrical solid, patch no.2

j	k	$B_{0,j,k}$	$B_{1,j,k}$	$B_{2,j,k}$	$w_{0,j,k}$	$w_{1,j,k}$	$w_{2,j,k}$
0	0	(9,0,2)	(27/2,0,2)	(18,0,2)	1	1	1
1	0	(9,0,3)	(27/2,0,3)	(18,0,3)	1	1	1
2	0	(9,0,4)	(27/2,0,4)	(18,0,4)	1	1	1
0	1	(9,2,2)	(27/2,2,2)	(18,2,2)	$1/\sqrt{2}$	$1/\sqrt{2}$	$1/\sqrt{2}$
1	1	(9,3,3)	(27/2,3,3)	(18,3,3)	$1/\sqrt{2}$	$1/\sqrt{2}$	$1/\sqrt{2}$
2	1	(9,4,4)	(27/2,4,4)	(18,4,4)	$1/\sqrt{2}$	$1/\sqrt{2}$	$1/\sqrt{2}$
0	2	(9,2,0)	(27/2,2,0)	(18,2,0)	1	1	1
1	2	(9,3,0)	(27/2,3,0)	(18,3,0)	1	1	1
2	2	(9,4,0)	(27/2,4,0)	(18,4,0)	1	1	1

Table A.4: Control points and weights for cylindrical solid, patch no.3

j	k	$B_{0,j,k}$	$B_{1,j,k}$	$B_{2,j,k}$	$w_{0,j,k}$	$w_{1,j,k}$	$w_{2,j,k}$
0	0	(0,2,0)	(9/2,2,0)	(9,2,0)	1	1	1
1	0	(0,3,0)	(9/2,3,0)	(9,3,0)	1	1	1
2	0	(0,4,0)	(9/2,4,0)	(9,4,0)	1	1	1
0	1	(0,2,-2)	(9/2,2,-2)	(9,2,-2)	$1/\sqrt{2}$	$1/\sqrt{2}$	$1/\sqrt{2}$
1	1	(0,3,-3)	(9/2,3,-3)	(9,3,-3)	$1/\sqrt{2}$	$1/\sqrt{2}$	$1/\sqrt{2}$
2	1	(0,4,-4)	(9/2,4,-4)	(9,4,-4)	$1/\sqrt{2}$	$1/\sqrt{2}$	$1/\sqrt{2}$
0	2	(0,0,-2)	(9/2,0,-2)	(9,0,-2)	1	1	1
1	2	(0,0,-3)	(9/2,0,-3)	(9,0,-3)	1	1	1
2	2	(0,0,-4)	(9/2,0,-4)	(9,0,-4)	1	1	1

Table A.5: Control points and weights for cylindrical solid, patch no.4

j	k	$B_{0,j,k}$	$B_{1,j,k}$	$B_{2,j,k}$	$w_{0,j,k}$	$w_{1,j,k}$	$w_{2,j,k}$
0	0	(9,2,0)	(27/2,2,0)	(18,2,0)	1	1	1
1	0	(9,3,0)	(27/2,3,0)	(18,3,0)	1	1	1
2	0	(9,4,0)	(27/2,4,0)	(18,4,0)	1	1	1
0	1	(9,2,-2)	(27/2,2,-2)	(18,2,-2)	$1/\sqrt{2}$	$1/\sqrt{2}$	$1/\sqrt{2}$
1	1	(9,3,-3)	(27/2,3,-3)	(18,3,-3)	$1/\sqrt{2}$	$1/\sqrt{2}$	$1/\sqrt{2}$
2	1	(9,4,-4)	(27/2,4,-4)	(18,4,-4)	$1/\sqrt{2}$	$1/\sqrt{2}$	$1/\sqrt{2}$
0	2	(9,0,-2)	(27/2,0,-2)	(18,0,-2)	1	1	1
1	2	(9,0,-3)	(27/2,0,-3)	(18,0,-3)	1	1	1
2	2	(9,0,-4)	(27/2,0,-4)	(18,0,-4)	1	1	1

Table A.6: Control points and weights for cylindrical solid, patch no.5

j	k	$B_{0,j,k}$	$B_{1,j,k}$	$B_{2,j,k}$	$w_{0,j,k}$	$w_{1,j,k}$	$w_{2,j,k}$
0	0	(0,0,-2)	(9/2,0,-2)	(9,0,-2)	1	1	1
1	0	(0,0,-3)	(9/2,0,-3)	(9,0,-3)	1	1	1
2	0	(0,0,-4)	(9/2,0,-4)	(9,0,-4)	1	1	1
0	1	(0,-2,-2)	(9/2,-2,-2)	(9,-2,-2)	$1/\sqrt{2}$	$1/\sqrt{2}$	$1/\sqrt{2}$
1	1	(0,-3,-3)	(9/2,-3,-3)	(9,-3,-3)	$1/\sqrt{2}$	$1/\sqrt{2}$	$1/\sqrt{2}$
2	1	(0,-4,-4)	(9/2,-4,-4)	(9,-4,-4)	$1/\sqrt{2}$	$1/\sqrt{2}$	$1/\sqrt{2}$
0	2	(0,-2,0)	(9/2,-2,0)	(9,-2,0)	1	1	1
1	2	(0,-3,0)	(9/2,-3,0)	(9,-3,0)	1	1	1
2	2	(0,-4,0)	(9/2,-4,0)	(9,-4,0)	1	1	1

Table A.7: Control points and weights for cylindrical solid, patch no.6

j	k	$B_{0,j,k}$	$B_{1,j,k}$	$B_{2,j,k}$	$w_{0,j,k}$	$w_{1,j,k}$	$w_{2,j,k}$
0	0	(9,0,-2)	(27/2,0,-2)	(18,0,-2)	1	1	1
1	0	(9,0,-3)	(27/2,0,-3)	(18,0,-3)	1	1	1
2	0	(9,0,-4)	(27/2,0,-4)	(18,0,-4)	1	1	1
0	1	(9,-2,-2)	(27/2,-2,-2)	(18,-2,-2)	$1/\sqrt{2}$	$1/\sqrt{2}$	$1/\sqrt{2}$
1	1	(9,-3,-3)	(27/2,-3,-3)	(18,-3,-3)	$1/\sqrt{2}$	$1/\sqrt{2}$	$1/\sqrt{2}$
2	1	(9,-4,-4)	(27/2,-4,-4)	(18,-4,-4)	$1/\sqrt{2}$	$1/\sqrt{2}$	$1/\sqrt{2}$
0	2	(9,-2,0)	(27/2,-2,0)	(18,-2,0)	1	1	1
1	2	(9,-3,0)	(27/2,-3,0)	(18,-3,0)	1	1	1
2	2	(9,-4,0)	(27/2,-4,0)	(18,-4,0)	1	1	1

Table A.8: Control points and weights for cylindrical solid, patch no.7

j	k	$B_{0,j,k}$	$B_{1,j,k}$	$B_{2,j,k}$	$w_{0,j,k}$	$w_{1,j,k}$	$w_{2,j,k}$
0	0	(0,-2,0)	(9/2,-2,0)	(9,-2,0)	1	1	1
1	0	(0,-3,0)	(9/2,-3,0)	(9,-3,0)	1	1	1
2	0	(0,-4,0)	(9/2,-4,0)	(9,-4,0)	1	1	1
0	1	(0,-2,2)	(9/2,-2,2)	(9,-2,2)	$1/\sqrt{2}$	$1/\sqrt{2}$	$1/\sqrt{2}$
1	1	(0,-3,3)	(9/2,-3,3)	(9,-3,3)	$1/\sqrt{2}$	$1/\sqrt{2}$	$1/\sqrt{2}$
2	1	(0,-4,4)	(9/2,-4,4)	(9,-4,4)	$1/\sqrt{2}$	$1/\sqrt{2}$	$1/\sqrt{2}$
0	2	(0,0,2)	(9/2,0,2)	(9,0,2)	1	1	1
1	2	(0,0,3)	(9/2,0,3)	(9,0,3)	1	1	1
2	2	(0,0,4)	(9/2,0,4)	(9,0,4)	1	1	1

Table A.9: Control points and weights for cylindrical solid, patch no.8

j	k	$B_{0,j,k}$	$B_{1,j,k}$	$B_{2,j,k}$	$w_{0,j,k}$	$w_{1,j,k}$	$w_{2,j,k}$
0	0	(9,-2,0)	(27/2,-2,0)	(18,-2,0)	1	1	1
1	0	(9,-3,0)	(27/2,-3,0)	(18,-3,0)	1	1	1
2	0	(9,-4,0)	(27/2,-4,0)	(18,-4,0)	1	1	1
0	1	(9,-2,2)	(27/2,-2,2)	(18,-2,2)	$1/\sqrt{2}$	$1/\sqrt{2}$	$1/\sqrt{2}$
1	1	(9,-3,3)	(27/2,-3,3)	(18,-3,3)	$1/\sqrt{2}$	$1/\sqrt{2}$	$1/\sqrt{2}$
2	1	(9,-4,4)	(27/2,-4,4)	(18,-4,4)	$1/\sqrt{2}$	$1/\sqrt{2}$	$1/\sqrt{2}$
0	2	(9,0,2)	(27/2,0,2)	(18,0,2)	1	1	1
1	2	(9,0,3)	(27/2,0,3)	(18,0,3)	1	1	1
2	2	(9,0,4)	(27/2,0,4)	(18,0,4)	1	1	1

References

[1] Akkerman I, Bazilevs Y, Calo VM , Hughes TJR, Hulshof S. The role of continuity in residual-based variational multiscale modeling of turbulence. Computational Mechanics 2008;41:371-78.

[2] Auricchio F, Beirao de Veiga L, Buffa A, Lovadina C, Reali A, Sangalli G. A fully "locking-free" isogeometric approach for plane linear elasticity problems: A stream function formulation. Comput Methods Appl Mech Eng 2007;197:160-72.

[3] Auricchio F, Beirao de Veiga L, Lovadina C, Reali A. The importance of the exact satisfaction of the incompressibility constraint in nonlinear elasticity: mixed FEMs versus NURBS-based approximations. Comput Methods Appl Mech Eng 2010;199:314-23.

[4] Azouz I, Shirazi SA. Evaluation of several turbulence models for turbulent flow in concentric and eccentric annuli, ASME J Energy Resources Tech 1998;120:268-75.

[5] Bazilevs Y, Beirao de Veiga L, Cottrell JA, Hughes TJR, Sangalli G. Isogeometric analysis: approximation, stability and error estimates for h-refine meshes. Mathematical Models and Methods in Applied Science 2006;16:1-60.

[6] Bazilevs Y, Calo VM, Cottrell JA, Hughes TJR, Reali A, Scovazzi G. Variational multiscale residual-based turbulence modeling for large eddy simulation of incompressible flows. Comput Methods Appl Mech Eng 2007;197:173-201.

[7] Bazilevs Y, Calo VM, Zhang JY, Hughes TJR. Isogeometric Fluid-Structure Interaction Analysis with Applications to Arterial Blood Flow. Computational Mechanics 2006;38:310-22.

[8] Bazilevs Y, Michler C, Calo VM, Hughes TJR. Weak Dirichlet boundary conditions for wall-bounded turbulent flows. Comput Methods Appl Mech Eng 2007;196:4853-62.

[9] Bazilevs Y, Michler C, Calo VM, Hughes TJR. Isogeometric variational multiscale modeling of wall-bounded turbulent flows with weakly-enforced boundary conditions on unstretched meshes. Comput Methods Appl Mech Eng 2010;199:780-90.

[10] Brooks AN, Hughes TJR. Streamline upwind/Petrov-Galerkin formulations for convection dominated flows with particular emphasis on the incompressible Navier-Stokes equations. Comput Methods Appl Mech Eng 1982;32:199-259.

[11] Calo VM. Residual-based Multiscale Turbulence Modeling: Finite Volume Simulation of Bypass Transition. PhD thesis, Department of Civil and Environmental Engineering, Standford University, 2004.

[12] Calo VM, Brasher N, Bazilevs Y, Hughes TJR. Multiphysics Model for Blood Flow and Drug Transport with Application to Patient-Specific Coronary Artery Flow. Computational Mechanics 2008;43:161-177.

[13] Chang K, Hughes TJR, Calo VM. Isogeometric Variational Multiscale Large-Eddy Simulation of Fully-developed Turbulent Flow over a Wavy Wall. Computers and Fluids 2011; submitted.

[14] Chung J, Hulbert GM. A time integration algorithm for structural dynamics with improved numerical dissipation: the generalized alpha-method. J Appl Mech 1993;60:371-75.

[15] Chung SY, Rhee GH, Sung HJ. Direct numerical simulation of turbulent concentric annular pipe flow Part 1: Flow field, Int J Heat and Fluid Flow 2002;23:426-40.

[16] Codina R, Principe J, Guasch O, Badia S. Time dependent subscales in the stabilized finite element approximation of incompressible flow problems. Comput Methods Appl Mech Eng 2007;196:2413-30.

[17] Collier NO, Pardo D, Paszyński M, Dalcín L, Calo VM. The cost of continuity: a study of the performance of isogeometric finite elements using direct solvers. Comput Methods Appl Mech Eng 2012; accepted for publication.

[18] Cottrell JA, Hughes TJR, Bazilevs Y. Isogeometric Analysis, Towards integration of CAD and FEA. Wiley, 2009.

[19] Cottrell JA, Hughes TJR, Reali A. Studies of Refinement and Continuity in Isogeometric Structural Analysis. Comput Methods Appl Mech Eng 2007;196:4160-83.

[20] Dedè L, Borden MJ, Hughes TJR. Isogeometric Analysis for topology optimization with a phase field model, ICES Report 11-29, The Institute for Computational Engineering and Sciences, The University of Texas at Austin 2011, Archives of Computational Methods in Engineering, accepted for publication.

[21] Duddu R, Lavier L, Hughes TJR, Calo VM. A finite strain Eulerian formulation for compressible and nearly incompressible hyper-elasticity using high-order NURBS elements. International Journal of Numerical Methods in Engineering 2012; 89:762-785.

[22] Escudier MP, Gouldson IW, Jones DM. Flow of shear-thinning fluids in a concentric annulus. Experiments in Fluids 1995;27:225-38.

[23] Gómez H, Calo VM, Bazilevs Y, Hughes TJR. Isogeometric analysis of the Cahn-Hilliard phase-field model. Comput Methods Appl Mech Eng 2008;197:4333-4352.

[24] Gómez H, Hughes TJR, Nogueira X, Calo VM. Isogeometric analysis of the isothermal Navier-Stokes-Korteweg equations. Comput Methods Appl Mech Eng 2010;199:1828.

[25] Holmen J, Hughes TJR, Oberai AA, Wells GN. Sensitivity of the scale partition for variational multiscale LES of channel flow. Phys Fluids 2004;16:824-27.

[26] Hossain S, Hossainy SFA, Bazilevs Y, Calo VM, Hughes TJR. Mathematical Modeling of Coupled Drug and Drug-Encapsulated Nanoparticle Transport in Patient-Specific Coronary Artery Walls. Computational Mechanics 2011; doi: 10.1007/s00466-011-0633-2.

[27] Hsu MC, Akkerman I, Bazilevs Y. High-performance computing of wind turbine aerodynamics using isogeometric analysis. Computers and Fluids 2011;49:93-100.

[28] Hughes TJR. Multiscale phenomena: Green functions, the Dirichlet-to-Neumann formulation, subgrid scale models, bubbles and the origins of stabilized methods. Comput Methods Appl Mech Eng 1995;127:387-401.

[29] Hughes TJR, Calo VM, Scovazzi G. Variational and multiscale methods in turbulence, in: W.Gutkowski,T.A. Kowalewski (Eds.), Proceedings of the XXI International Congress of Theoretical and Applied Mechanics (IUTAM), Kluwer, 2004.

[30] Hughes TJR, Cottrell JA, Bazilevs Y. Isogeometric analysis: CAD, finite elements, NURBS, exact geometry, and mesh refinement. Comput Methods Appl Mech Eng 2005;194:4135-95.

[31] Hughes TJR, Franca LP, Hulbert G. A new finite element formulation for computational fluid dynamics: VIII. The Galerkin least squares method for advective-diffusive equations. Comput Methods Appl Mech Eng 1989;73:173-89.

[32] Hughes TJR, Mallet M. A few finite element formulation for fluid dynamics: III. The generalized streamline operator for multidimensional advective-diffusive systems. Comput Methods Appl Mech Eng 1986;58:305-28.

[33] Hughes TJR, Mazzei L, Jansen KE. Large-eddy simulation and the variational multiscale method. Comp Vis Sci 2000;3:47-59.

[34] Hughes TJR, Mazzei L, Oberai AA, Wray AA. The multiscale formulation of large eddy simulation: decay of homogenous isotropic turbulence. Phys Fluids 2001;13:505-12.

[35] Hughes TJR, Oberai AA, Mazzei L. Large eddy simulation of turbulent channel flows by the variational multiscale method. Phys Fluids 2001;13:1784-99.

[36] Hughes TJR, Reali A, Sangalli G. Duality and Unified Analysis of Discrete Approximations in Structural Dynamics and Wave Propagation: Comparison of p-method Finite Elements with k-method NURBS. Comput Methods Appl Mech Eng 2008;197:4104-24.

[37] Hughes TJR, Sangalli G. Variational multiscale analysis: The fine-scale Green's function, projection, optimization, localization, and stabilized methods. SIAM Journal on Numerical Analysis 2007;45:539-57.

[38] Hughes TJR, Scovazzi G, Franca LP. Multiscale and stabilized methods, in: E. Stein, R. de Borst, T.J.R. Hughes (Eds.), Encyclopedia of Computational Mechanics, Computational Fluid Dynamics,Vol. 3, Wiley, 2004.

[39] Hughes TJR , Wells GN, Oberai AA, Wray AA. Energy transfers and spectral eddy viscosity of homogeneous isotropic turbulence: comparison of dynamic Smagorinsky and multiscale models over a range of discretizations. Phys Fluids 2004;16:4044-52.

[40] Jansen KE, Whiting CH, Hulbert GM. A generalized alpha-method for integrating the filtered Navier–Stokes equations with a stabilized finite element method. Comput Methods Appl Mech Eng 1999;190:305-19.

[41] Kim J, Moin P, Moser R. Turbulent statistics in fully developed channel at low Reynolds number, J Fluid Mech 1987;177:617-41.

[42] Koobus B, Farhat C. A variational multiscale method for the large eddy simulation of compressible turbulent flow on unstructed meshes – applications to vortex shedding. Comput Methods Appl Mech Eng 2004;193:1367-83.

[43] Lawn CJ, Elliott CJ. Fully Developed Turbulent Flow through Concentric Annuli, Central Electricity Generating Board Report RD/B/N/1878, United Kingdom, 1971.

[44] Liu NS, Lu XY. Large eddy simulation of turbulent concentric annular channel flows. Int J Num Meth Fluids 2004;45:1317-38.

[45] Nouri JM, Umur H, Whitelaw JH. Flow of Newtonian and non-Newtonian fluids in concentric and eccentric annuli. J Fluid Mech 1993;253:617-41.

[46] Piegl L, Tiller W. The NURBS book, Monographs in visual communication, second ed., Springer-Verlag, New York, 1997.

[47] Ramakrishnan S, Collis SS. Turbulent control simulation using the variational multiscale method. AIAA journal 2004;42:745-53;

[48] Reali A. An isogeometric analysis approach for the study structural vibrations. Journal of Earthquake Engineering 2006;10:1-30.

[49] Rehme K. Turbulence measurements in smooth concentric annuli with small radius ratios. J Fluid Mech 1975;72:189-206.

[50] Verhoosel CV, Scott MA, Hughes TJR, de Borst R. An isogeometric analysis approach to gradient damage models. International Journal for Numerical Methods in Engineering 2011;86:115134.

[51] White FM. Fluid Mechanics, third ed., Mc Graw–Hill, New York, 1994.

[52] Zhang Y, Bazilevs Y, Goswami S, Bajaj CL, Hughes TJR. Patient-specific vascular NURBS modeling for isogeometric analysis of blood flow. Comput Methods Appl Mech Eng 2007;196:2943-59.